



Single-dish 1-cm-band radio photometry of protoplanetary discs: few centimetre-sized dust grains?

Jane S. Greaves ¹★ and Brian Mason ²

¹*School of Physics & Astronomy, Cardiff University, 4 The Parade, Cardiff CF24 3AA, UK*

²*National Radio Astronomy Observatory, 520 Edgemont Road, Charlottesville, VA 22903, USA*

Accepted 2022 March 25. Received 2022 March 25; in original form 2021 March 8

ABSTRACT

Radio-wavelength observations of protoplanetary discs can show whether large dust grains (pebbles) have formed on the pathway to aggregation of planetary cores. The 100-m Green Bank Telescope was used to make a four-subband (26–40 GHz) photometric survey of the Taurus and Ophiuchus regions, which is nearly complete for class II systems above fixed millimetre-flux thresholds. There is evidence of anomalous microwave emission in 40 per cent of the systems, indicating that radio observations of protoplanetary discs need good spectral coverage to distinguish the presence of dust. At most, one-quarter of the systems are seen to host pebbles, of radii as large as 1 cm. The lack of pebble-dominated systems suggests that this is a short-lived phase in particle size evolution, and/or that pebbles only grow in limited areas of the disc. Either case supports models where grains of centimetre size rapidly fragment and/or drift towards the star, potentially feeding growing planets. In the best-fitting systems, including the 26–40 GHz data raises the detected dust mass by up to an order of magnitude, and the mass distribution of the discs may be flatter. Both of these phenomena could help to solve the ‘missing mass’ problem, where the solid budget in protoplanetary discs is compared with the substantial requirements of extrasolar-planet systems.

Key words: radio continuum; planetary systems.

1 INTRODUCTION

Long-wavelength photometry provides an efficient way to measure the mass budgets in solids within protoplanetary discs. The continuum emission is typically a Rayleigh–Jeans tail to a blackbody function, but modified by the emissivity of the particles. F_ν , the flux as a function of frequency ν , can be described by $F_\nu \propto \nu^{2+\beta}$, where the index is 2 for a blackbody and β modifies this slope to a more steeply declining ‘greybody’. The underlying reason can be that grains are inefficient emitters of waves larger than about their own circumference (e.g. Draine 2006). Hence, the spectral energy distribution (SED) declines with an emissivity κ , where $\kappa \propto \nu^\beta$ can characterize a deficit of large grains. Analysis of the SEDs including the emissivity can then give a mass in solids present, which can be compared with the mass needed to construct planet cores. Greaves & Rice (2010, 2011), Najita & Kenyon (2014), Manara, Morbidelli & Guillot (2018), and Tychoniec et al. (2020) have noted some problems and solutions in the apparent mass deficits in discs when compared with requirements for forming populations of extrasolar planets.

Radio-wavelength imaging of protoplanetary discs was pioneered by the Disks@EVLA (Expanded Very Large Array) survey, as described by Chandler (2007). At about the same time, we undertook a photometric survey of protoplanetary discs using the 100-m Green Bank Telescope (Greaves 2007). The aim was to search for evidence of grain growth in a flux-limited sample of disc systems. This growth is important on the pathway towards solid planetary cores,

but could be frustrated by grain drift or fragmentation (see e.g. fig. 4 of Birnstiel, Fang & Johansen 2016). On the other hand, grains might already be changing their state in pre-stellar cloud cores and protostellar envelopes, with strong evidence for low β in some cases (Mason et al. 2020, referencing grain physics of Paradis et al. 2011; Galametz et al. 2019).

Our analysis of the Green Bank Telescope (GBT) data has been slowed down by the problem posed by non-power-law SEDs – eventually solved by the identification of anomalous microwave emission (AME) in at least one of the discs (Greaves et al. 2018). We here analyse the remainder of the GBT sample and draw conclusions about the prevalence of large grains in the protoplanetary systems.

2 SURVEY DATA

2.1 Source selection

The original aim was a complete sample of ‘class II’ disc-dominated young star systems in the nearby northern Taurus and Ophiuchus regions, based on photometric surveys at the 1.3 mm wavelength, as collated by Andrews & Williams (2005, 2007). With then-canonical distances to these regions of 140 and 160 pc, respectively, our Tau and Oph flux thresholds were 100 and 90 mJy, aiming to detect a ‘minimum-mass solar nebula’ (MMSN) of gas and dust.¹ Our GBT survey was close to complete under these assumptions, with

¹These definitions relied on one MMSN being 0.02 solar masses (Davis 2005) and a gas-to-dust mass ratio of 100 being inherited unaltered from the interstellar medium.

* E-mail: greavesj1@cardiff.ac.uk

Table 1. Comparison of Disks@EVLA and GBT- K_a /CCB fluxes, with respective wavelengths in brackets. Errors in the ratios are propagated quadratically from the errors in the flux measurements.

Target	Flux ratios (EVLA/GBT)	EVLA reference
AS 209	1.3 ± 0.3 (8.0/7.8 mm), 0.8 ± 0.2 (9.8/9.6 mm)	Tazzari et al. (2016)
FT Tau	0.9 ± 0.2 (8.0/7.8 mm), 1.2 ± 0.4 (9.8/9.6 mm)	Tazzari et al. (2016)
DoAr 25	2.4 ± 1.1 (8.0/7.8 mm), 1.2 ± 0.2 (9.8/9.6 mm)	Pérez et al. (2015)

30 targets. The system names of Andrews and Williams are mostly adopted here, but we note commonly used alternate names.

Subsequent parallax data and more complete spectral classifications mean that the sample is now slightly more diverse in mass sensitivity and evolutionary state than the original intent. In Taurus, IC 2087 IR and MHO 1/2 may be less evolved class I/II systems (Furlan 2011; Baldovin-Saavedra et al. 2011), while DM Tau, GM Aur, and WSB 42 may be later-stage transition discs (Furlan et al. 2011; van der Marel et al. 2016). Two errors also occurred in our observation set-up: LFAM 30 (class I) was targeted instead of LFAM 3 (not affecting completeness: Appendix A), while the class II UZ Tau system was accidentally omitted. The classes refer to the primary star in the system, with a substantial fraction of systems being multiples (e.g. Harris 2013); the GBT beam would include any discs around secondary stars. Revised distances mean that three of the observed systems require adjustments of 40–90 per cent in disc masses (Section 3.7) compared with older works.

2.2 Observations

The GBT observations were made in two runs on 2007 April 21 and 26, using the K_a -band receiver with the Caltech Continuum Backend (CCB). The CCB provides high sensitivity via optimized detector circuits and the capability to rapidly beam switch to suppress instrumental gain fluctuations. The K_a /CCB combination provides four frequency subbands (0, 1, 2, and 3) simultaneously, at 26–29.5, 29.5–33, 33–36.5, and 36.5–40 GHz, respectively, i.e. contiguous wavelength coverage over 7.5–11.5 mm. The typical flux error (standard deviation) achieved in the photometry was around a tenth of a mJy in each subband, as tabulated in Section A1 of Appendix A.

GBT- K_a /CCB photometry nods on the sky between on and off source positions with four 10-s phases in a 70-s observation; this was repeated five to nine times for each of our sources. During the second run, on Ophiuchus, conditions deteriorated and large scatter was observed within some observations for the final five targets; see Appendix A, Section A2, for details. For the remaining 25 targets, coadded fluxes were extracted using the GBTIDL package (<http://gbitdl.nrao.edu/>).

The angular resolution was 24 arcsec FWHM (~ 3000 au) at a representative frequency of 31 GHz, so the environment of each disc system is included. If grains begin to grow early on, then the GBT fluxes could include large grains in remnant envelopes/cores, and so could be higher than interferometric fluxes that tend to resolve out these scales. However, no such effect is seen in the three sources in common with Disks@EVLA, with fluxes published at very similar wavelengths (Table 1). None of these EVLA/GBT flux ratios are

Table 2. Results of weighted linear least-squares regression to the four K_a subband fluxes. In case subband fluxes were slightly correlated, covariances were included in fitting (see text). The spectral index is for $F_\nu \propto \nu^\alpha$; ‘S/N’ denotes the signal-to-noise ratio. The upper section of the table lists sources with no evidence of spectral curvature in the K_a band (correlation coefficients $r = 0.63$ – 1.00), and the lower section lists sources with evidence of curvature ($r = 0.10$ – 0.74 ; see the text for other selection criteria). Within each section, sources are ordered by region, and then by decreasing spectral index. Classifications listed in brackets include class I, class II, transition disc (TD), and Herbig AeBe (HAe, for luminous stars, generally equivalent to class II); any secondary stars in the system may not share the same class.

Region	Target (IR class)	S/N $F(K_a)$	Index $\alpha(K_a)$	Correlation coefficient (r)
Taurus	FT Tau (II)	2.7	3.2 ± 0.5	0.98
	LkCa 15 (II)	3.2	2.7 ± 0.5	0.97
	MHO1/2 (I/II)	4.4	1.9 ± 0.2	0.99
	DL Tau (II)	4.9	1.7 ± 0.1	1.00
	AB Aur (HAe)	6.3	1.4 ± 0.4	0.93
	Haro 6-13 (II)	5.7	1.3 ± 0.4	0.93
	IC 2087 IR (I/II)	7.2	1.2 ± 0.1	1.00
	DR Tau(II)	7.6	0.7 ± 0.6	0.63
	Ophiuchus	WSB 31 (II)	4.2	1.8 ± 0.8
WSB 42 (II/TD)		10.9	0.9 ± 0.1	0.99
Taurus	DO Tau (II)	3.8	1.7 ± 1.1	0.73
	GM Aur (II/TD)	5.6	1.3 ± 1.2	0.58
	CI Tau (II)	2.5	0.6 ± 1.3	0.29
	GG Tau (II)	23.7	0.0 ± 0.2	0.37
	T Tau (II)	36.1	-0.2 ± 0.1	0.74
	V892 Tau (HAe)	5.7	-0.5 ± 0.9	0.33
Ophiuchus	AS 209 (II)	3.0	2.4 ± 1.6	0.72
	DoAr 25 (II)	4.3	1.2 ± 1.5	0.48
	AS 205 (II)	13.7	0.2 ± 0.4	0.29
	VSSG 23 (HAe)	2.8	-0.4 ± 2.4	0.10

below 1, given the measurement errors.² One EVLA/GBT flux ratio is nominally just above 1, at ≥ 1.3 for one wavelength observed for the faint DoAr 25 system. This could indicate some temporal variability in this system that likely has a mix of emission mechanisms (see discussion in the following, and Table 2). If these three sources are representative, the low resolution of our study should not affect later conclusions about the spectral indices.

Background or associated sources could in principle still complicate the flux analysis. However, a density of ≥ 1 mJy extragalactic radio sources in the K_a band of only ~ 4 degree⁻² has been inferred (Majid & Bagri 2006). As the total sky area we covered with the GBT was $\approx 10^{-3}$ degrees², it is unlikely we saw even one extragalactic source at the mJy flux levels of interest. Regarding stellar companions, inspection of 30–43 GHz images of hierarchical multiples in the Disks@EVLA archive shows primary-disc:secondary-disc flux ratios typically $\gtrsim 5$. The ‘main’ disc should therefore dominate our GBT fluxes even though the multiple discs are not resolved. The only clear exception is the MHO 1/2 system where the discs are of similar brightness at 34 GHz with EVLA. In our literature compilation, we combined the two fluxes for the only data point where these discs were resolved (Section A1 in Appendix A: 51 + 30 mJy signals at

²Systematic uncertainties are not included in Table 1; absolute fluxes were set using primary calibrators 3C 48 and 3C 147, and their fluxes tabulated at the time at GBT may have been off by ~ 10 per cent compared with more recently established values (Perley & Butler 2013; <https://www.gb.nrao.edu/GBTICAL/>).

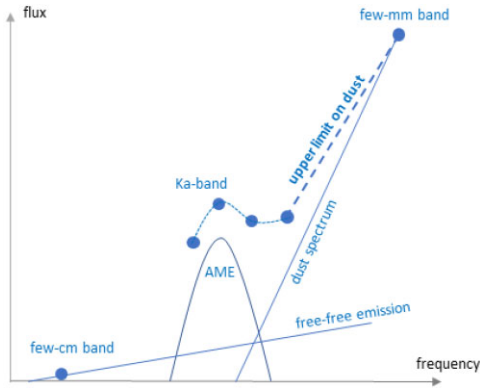


Figure 1. Sketch of method to extract a dust upper limit in the presence of multiple emission mechanisms. The dashed line represents the most realistic estimate for the dust spectrum, as contributions from anomalous microwave emission and free-free emission are expected to be least in the highest frequency K_a subband.

102.5 GHz). The analysis therefore de facto treats these two discs as having similar properties.

3 RESULTS

3.1 System characterization

Photometry results are obtained from the four subbands separately, for each target. From these four measurements, we can establish an in-band spectral index, $\alpha(K_a)$, and a noise-weighted flux representing the K_a band as a whole, $F(K_a)$. $F(K_a)$ can also be used with literature data to establish spectral indices connecting to short-millimetre and long-centimetre wavebands. These long-lever-arm indices help to establish the emission mechanisms present in the target systems.

The chief difficulty is that if more than two emission mechanisms are present, they cannot be characterized using only four K_a -subband flux points. Dust emission and free-free electron transitions are both described by power laws, with an index and amplitude each, while AME is described by a central frequency and amplitude (and it needs three points to establish a peaked nature). Therefore, if all three phenomena are present, there are six free parameters, which cannot be fitted with only four measurements.

Given this complexity, there will be systems where we can only set upper limits to the K_a -band dust contribution. We assume that the signal in the highest frequency subband (36.5–40 GHz) sets an upper limit of K_a -band dust flux, as this subband will be the most dust dominated for $F_\nu \propto \nu^{2+\beta}$ when any free-free emission and/or AME are more significant in the lower-frequency sub-bands (Fig. 1). The dust spectral index estimated between K_a subband 3 (36.5–40 GHz, 7.8 mm) and a 3-mm-band flux is then a lower limit, allowing steeper spectra that could arise from smaller grains.

The in-band indices $\alpha(K_a)$ were obtained from a weighted linear least-squares regression of $\ln(F)$ against $\ln(\text{frequency})$. Results are listed in Table 2, for systems detected at $>2.5\sigma$ in $F(K_a)$ and having at least one subband at $\geq 3\sigma$. In case the subband fluxes were somewhat correlated, the fits used variances σ_i^2 that have been increased for each subband i to $(\sigma_i^2 + 0.5\sigma_i\sigma_j + 0.5\sigma_i\sigma_k + 0.5\sigma_i\sigma_m)$. The effect on the derived index is generally ≤ 0.1 and in all cases less than the stated error on the index.

We examined the results for characteristics of interest, including the following:

(i) spectral indices $\alpha < 3$, often regarded as an indicator of dust growth, i.e. between $\alpha \sim 4$ for very small interstellar grains and $\alpha \sim 2$ for blackbodies much larger than the observing wavelength.

(ii) values of $\alpha \sim 0-1$ suggesting free-free emission (potentially tending towards 2 in cases of high optical depth).

(iii) evidence of non-power-law systems, via an excess flux in subband 1 or 2 compared with the average flux of subbands 0 and 3. Our conditions for a peak being significant were (a) an excess $\geq 2\sigma$ in normalized flux, with σ being the measurement uncertainty for the peak subband, and/or (b) a power-law correlation coefficient $r < 0.4$.

The 30 systems in our survey are then classified into groups:

- A: uncertain K_a flux (observed in poor conditions) – 5 sources.
- B: upper limits, all having $F(K_a) \leq 1.5\sigma$ – 5 sources.
- C: candidate AME, based on K_a -band curvature – 10 sources.
- D: Free-free dominated – 1 source.
- E: Dust signal present or possible at K_a band – 9 sources.

Overall, the GBT survey suggests AME could be present in 40 per cent of our sample (10/25 systems), hindering the detection of dust signals at the K_a band. Around a third (9/25) of our systems are candidates for dust detection. We next characterize the systems in each class.

3.2 Systems with uncertain flux (group A)

The last five Ophiuchus targets were observed as conditions deteriorated. Each observation was visually examined for jumps in signal level. After rejecting bad observations, noise-weighted subband averages were made of the remaining observations, followed by noise-weighted averages over the four subbands, to estimate K_a -band fluxes (Table 3). These are regarded as not of significant quality for our scientific purposes, so no spectral indices are listed.

3.3 Systems with upper limits (group B)

Five systems have $F(K_a) \leq 1.5\sigma$, after making a noise-weighted average of the four subband fluxes. Limits can be placed on the dust spectral indices of these systems; Table 3 lists $\alpha(7.8-3)$ and $\alpha(9-3)$ obtained by fitting a power law between the mean-plus-sigma value of $F(7.8$ or 9 mm) and $F(3$ mm), a flux in the 3 mm band (Table A1). The $\alpha(7.8-3)$ index is listed only for two cases where flux was detected above 3σ in the 7.8 mm subband, while the mean $F(K_a)$ is not detected (attributed to a steep spectrum).

None of these systems can have α below 3, which could indicate that large grains are present. The average K_a signal of the five systems is marginally detected, at 0.15 ± 0.07 mJy (mean \pm standard error), so dust emission can rarely exceed tenth-of-mJy levels in this group. As the mean 3 mm band flux is ≈ 20 mJy, an average K_a -band dust flux of >0.7 mJy would be expected for α below 3. As this is not seen, large grains cannot be prevalent in this group of sources.

3.4 Systems with candidate anomalous microwave emission (group C)

In Greaves et al. (2018), we showed that AME is present in the V892 Tau system, combining the GBT- K_a results with other radio-wavelength data. We now identify nine other systems with some evidence of K_a -band spectral curvature, with a $\geq 2\sigma$ flux excess and/or a poor fit to any power law (Table 2). Fig. 2 presents the average spectrum for eight systems, after normalizing to peak

Table 3. Results for sources where a dust spectrum cannot be fitted. $F(K_a)$ is the noise-weighted mean flux from the four subbands; the mean can be negative where a faint source was not detected, due to random measurement fluctuations. Spectral indices α are for power laws connecting the net K_a band (‘9 mm’) flux or the K_a subband 3 (7.8 mm) flux to a literature flux in the 3 mm band (Table A1). Indices are all lower limits because non-dust emission cannot be subtracted (Fig. 1). In each section, sources are ordered by region and then by decreasing 1.3 mm flux. Upper section: sources with uncertain K_a -band flux where some observations were rejected (Appendix A). Numbers in brackets in the first column indicate the number of usable observations. Middle section: sources with upper limits on K_a -band flux from the combined subbands. The spectral index limits are calculated from mean flux + positive error at K_a and mean flux at 3 mm. For two sources, the net K_a flux was not detected but the 7.8 mm subband flux is $\geq 3\sigma$. Lower section: sources with evidence of AME. Sources in brackets: for CI Tau, mean plus positive error is adopted at 7.8 mm because the mean signal is very close to zero; for T Tau, α is a weak limit as the system is heavily free-free dominated.

Region	Target	$F(K_a)$ (mJy)	$\alpha(7.8-3)$ [$\alpha(9-3)$]
Group A:			
Ophiuchus	Wa Oph 6 (6/7)	1.40 ± 0.30	–
	GSS 26 (4/7)	0.03 ± 1.04	–
	DoAr 44 (3/7)	0.78 ± 4.39	–
	LFAM 30 (2/7)	1.72 ± 0.68	–
	RNO 91 (4/7)	1.44 ± 0.88	–
Group B:			
Taurus	CY Tau	0.27 ± 0.29	$>3.3 \pm 0.2$ [>3.2]
	DM Tau	0.14 ± 0.10	– [>3.5]
	CW Tau	-0.09 ± 0.16	– [>4.2]
Ophiuchus	GSS 39	0.16 ± 0.18	$>4.7 \pm 0.4$ [>4.7]
	WSB 60	0.26 ± 0.17	– [>3.5]
Group C:			
Taurus	GG Tau	1.05 ± 0.04	>4.1
	T Tau	13.06 ± 0.36	(>1.3)
	GM Aur	0.33 ± 0.06	>3.9
	V892 Tau	1.58 ± 0.28	>3.9
	CI Tau	0.17 ± 0.07	(>5.0)
Ophiuchus	DO Tau	0.79 ± 0.21	>3.3
	AS 205	1.44 ± 0.10	>3.4
	AS 209	0.69 ± 0.23	>3.5
	DoAr 25	0.64 ± 0.15	>4.5
	VSSG 23	0.35 ± 0.13	>3.7

subband signal per source and then averaging sources (unweighted). The peak flux was in subband 2 in five cases and in subband 1 in three cases. The T Tau system is plotted separately; the peak is $\approx 6\sigma$ but is a small contributor to the total (free-free dominated) flux.

Errors in telescope pointing could give rise to apparently lower flux densities at shorter wavelengths, potentially mimicking the SED turnover seen in our measurements. The GBT pointing, however, is sufficiently accurate that this is not a concern. The typical GBT 2D RMS (referenced) pointing offset is 2.7 arcsec (Balsler, Nikolic & Prestage 2006), which would suppress the 38.25 GHz flux density by ~ 1 per cent relative to the next lowest frequency channel (34.75 GHz). We also rule out a free-free spectrum with a turnover produced by the emission transitioning from optically thin to optically thick – this produces a steep slope on the low-frequency side of the peak, rather than on the high side as suggested by Fig. 2.

Fig. 2 shows 10 systems in all that have evidence of spectral curvature in the K_a band – the SEDs are distinctly different from example trends (dashed lines) of either free-free or dust spectra. Similarities of the new candidates to the V892 Tau spectrum suggest that AME may commonly originate from nanometre-scale particles

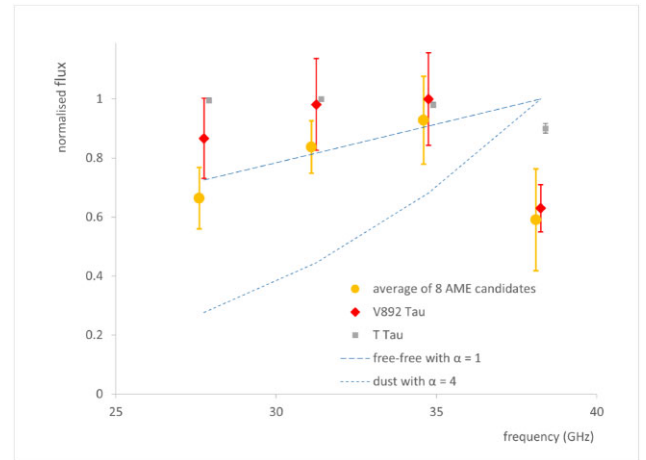


Figure 2. Net normalized spectrum (yellow circles) of eight AME candidates, compared with the AME-confirmed system V892 Tau (red diamonds; Greaves et al. 2018). The bright T Tau system is also shown (grey squares); free-free emission dominates but curvature is significant. Points are separated in frequency for clarity only. Error bars are measurement uncertainty for the red and grey points, and average measurement uncertainty for the yellow points (smaller values than the standard deviation among the eight systems; see Table A1). The blue dashed curves illustrate examples of power-law spectra.

(Greaves et al. 2018). However, the new AME candidates are difficult to characterize further due to sparse frequency sampling, modest signal to noise, and non-contemporaneous ancillary fluxes.

Adopting the approach of Fig. 1, Table 3 lists lower limits on the 7.8–3 mm spectral index that could be attributed to dust. Apart from the weak-limit case of the T Tau system, none of these indices can be below 3, so large grains are not prevalent in these systems.

3.5 Systems dominated by free-free emission (group D)

K_a -band spectral indices $\lesssim 1$ suggest dominant free-free emission for 10 of the Table 2 sources; however, 6 of these were discussed in the preceding section as AME candidates. The remaining four objects are IC 2087 IR, DR Tau, Haro 6-13, and WSB 42, all with K_a -in-band indices of ~ 1 . IC 2087 IR has surrounding or nearby cloud/core emission (Furlan 2011; Tokuda et al. 2020), and there is only an upper limit to 3-mm flux (Table A1). As the 1.3-mm flux could arise from cloud/core emission, it is not possible to extract a dust signal for the disc. The millimetre/centimetre spectrum is rather flat (Table A1), suggesting that free-free emission dominates, but any further analysis is difficult. The remaining three systems in this group appear free-free dominated in the K_a band, but have dust-like $\alpha(7.8-3)$ of 2.5–3.8, so are included in the group that follows.

3.6 Systems with dust present or possible (group E)

For the remaining nine systems, we fit a spectral energy distribution to wavebands at 3 mm and longer, with two power laws representing dust and free-free emission (Table 4). For N flux measurements, the number of degrees of freedom is $\text{dof} = N - 4$ and we calculate reduced chi-squared values χ_r^2 from $(1/\text{dof}) \sum[(\text{data model})^2/\text{data error}^2]$. For consistency, we have adopted survey data from the literature in preference to one-off studies, including Very Large Array (VLA) results at 4.5 and 7.5 GHz (Dzib et al. 2013, 2015), 5.8 GHz (Disks@EVLA archive), and 8.9 GHz (Zapata, Rodríguez & Palau 2017); our GBT photometry at 26–40 GHz; and results from

Table 4. Results of the SED fitting for sources that are dust candidates. The listing is by region and then ordered by decreasing 1.3 mm flux. Solutions are listed for the fits with smallest χ_r^2 (shown in Fig. 3), followed by $\alpha(\text{dust})$ in brackets that are the lowest values allowed within 68 per cent confidence bounds [$\alpha(\text{wind})$ differs from the tabulated value by up to 0.2 for these solutions]. The 68 per cent confidence χ_r^2 is 1.17, except for LkCa 15 with χ_r^2 of 0.99 for only 1 degree of freedom. The step size in testing index values was 0.1. The fraction of the 7.8 mm emission due to dust in the best-fitting model is listed as $f_d(7.8)$; values in brackets are for the 68 per cent confidence solutions. The negative spectral index in square brackets is discussed in the text.

Region	Target	$\alpha(\text{wind})$	$\alpha(\text{dust})$	$f_d(7.8)$	χ_r^2
Taurus	MHO 1/2	0.8	3.3	0.82	3.26
	DL Tau	[−1.1]	3.7 (≥ 3.5)	0.96 (0.97)	0.45
	LkCa 15	0.6	3.6 (≥ 3.5)	0.81 (0.84)	0.75
	DR Tau	0.0	2.7	0.92	1.09
	FT Tau	0.0	3.0 (≥ 2.9)	0.94 (1.00)	0.39
	Haro 6-13	1.3	3.0 (≥ 2.9)	0.42 (0.47)	0.91
Ophiuchus	AB Aur	0.7	5.0 (≥ 3.6)	0.12 (0.46)	0.69
	WSB 31	0.3	5.0	0.60	5.40
	WSB 42	1.5	5.0	0.27	2.93

Australia Compact Telescope Array (ATCA), Combined Array for Research in Millimeter-wave Astronomy (CARMA), and Plateau de Bure Interferometer (PdBI) at 91–113 GHz (Piétu et al. 2006; Ricci et al. 2010b, 2012; Kwon et al. 2015). Data at 140–240 GHz are used later for checking spectral fits (Table A1). Where the available data are heterogeneous, we gave preference to lower resolution observations, to better match our GBT data.

Fig. 3 shows the SED fits and Table 4 lists the spectral indices derived for the nine dust candidate systems. The indices given are the solutions at minimum χ_r^2 , plus the lowest allowed $\alpha(\text{dust})$ where other solutions exist within a 68 per cent confidence threshold. Three of the systems are poorly fitted, because it is not possible to fit all the non-contemporaneous data at low frequencies. In most other cases, the dust spectral index for the best fit and the 68 per cent confidence fit agree within ≤ 0.2 ; the exception is AB Aur, where the fraction of 7.8 mm emission due to dust is uncertain.

The number of systems in our GBT survey with evidence of large grains remains small. In Table 4, only 3 out of 9 systems can have $\alpha(\text{dust}) \lesssim 3$. Combining the results of Tables 3 and 4, only 3 out of 23 systems have dust index fits or limits that are consistent with this empirical indicator for large grains – i.e. only ~ 15 per cent of our class-II-dominated sample.

The free–free indices are within the expected bounds, with $\alpha(\text{wind})^3$ in Table 4 of 0.0–1.5. The exception is DL Tau, where a negative index is needed to fit the low-frequency data. This could be characteristic of a non-thermal mechanism – see Ubach et al. (2017) and Lommen et al. (2009) for discussion – but the fit is insecure given the up to 50 per cent temporal variability in this source (Dzib et al. 2015).

The dust indices were allowed to range in the interval from 2 (i.e. large blackbody grains) up to a maximum of 5. Generally, $\alpha(\text{dust})$ is not expected to exceed ~ 4 (for very small grains), but steeper slopes of κ_ν may occur locally in a spectrum for some particle size distributions (e.g. Cuzzi, Estrada & Davis 2014, fig. 8: indices up to ≈ 4.5). Solutions were found for the ≤ 3 -mm dust emission in all

systems; 1.3 mm and 2 mm flux points are not fitted here, given that dust emission from massive discs could become optically thick at these wavelengths.

Fig. 3 also shows model fits to the nine dust candidate systems, based on mass opacities κ_ν that are realistic for protoplanetary discs. We use values plotted by Cuzzi et al. (2014: fig. 8)⁴ for Mie theory calculations for solid particles that have a standard compositional mixture (derived from Pollack et al. 1994). Two different grain size distributions are presented by Cuzzi et al. (2014), with indices $q = 2.0$ and 3.1 for number densities of particles described by $n(r) = n_0 r^{-q}$; the resulting mass and opacities differ by ≤ 35 per cent with other parameters held constant, a variation difficult to distinguish in our data.

We primarily use the 7.8–3 mm slope of wind-subtracted fluxes to constrain the largest grain size a_{max} that is present in our nine systems, considering also the trend towards 2 and 1.3 mm wavelengths to assess fits that are similar. The grain size distributions in Cuzzi et al. (2014) are truncated at a_{max} of 0.01, 0.1, 1, and 10 mm, with $\alpha(\text{dust})$ of 3.0–4.3 possible over the wavelength range 3–7.8 mm. For these regimes, we find the two fitted fluxes are offset from the best model by at most ± 60 per cent, with only two out of nine cases worse than ± 30 per cent. More refined solutions (calculating κ_ν for intermediate size limits) are probably not warranted given our modest signal to noise.

The choice of a_{max} between 1 mm and 1 cm affects the mass–opacity by 0.5 dex, in the sense that higher disc masses are required to produce the observed dust flux when the size distribution truncates at the smaller particle size. Masses would be even higher with a_{max} of 10 or 100 μm (Cuzzi et al. 2014), but no solutions favoured these values.

3.7 Disc masses

We can finally estimate disc masses or limits for 23 systems, 9 with well-fitted SEDs and 14 where the K_a -band dust flux is an upper limit (for detectability or AME-contamination reasons). The disc masses are calculated according to

$$M_d = F_\nu d^2 / \kappa_\nu B_\nu(T) \quad (1)$$

and are listed in Table 5. The masses refer to the total of gas and dust present, assuming 1.4 per cent of the mass is in the solid components of the compositional mix (Cuzzi et al. 2014) and that none of the gas in the disc that was inherited from pre-stellar stages has been dispersed.

Table 5 also lists masses previously derived when fluxes at up to 1.3 mm wavelengths were available (Andrews & Williams 2005, 2007) and when 3 mm signals were later surveyed (Ricci et al. 2010a,b). Our 7.8 mm fluxes are better able to distinguish the presence or absence of centimetre-sized ‘pebbles’, and the expectation is that the overall mass budgets for planet formation may be larger if such particles are present.

All these studies we refer to have fitted dust SEDs to estimate suitable κ -values. Ricci et al. (2010a,b) based κ -values on materials data from Pollack et al. (1994), the same source as we use here (via Cuzzi et al. 2014). Ricci et al. (2010a,b) list masses for size indices q of 2.5 and 3, and we averaged these two (typically similar) results to generate the mass column in our Table 5. The effects of different q on κ are subtle (Cuzzi et al. 2014: fig. 8), so even where $q = 2$

³For brevity, we refer to the non-dust emission as a wind signature, i.e. free–free electron emission from outflowing ionized gas, but there could be another origin, such as an H II region.

⁴Similar calculations were made by d’Alessio, Calvet & Hartmann (2001), so results for slightly different grain size distributions and temperatures can be compared.

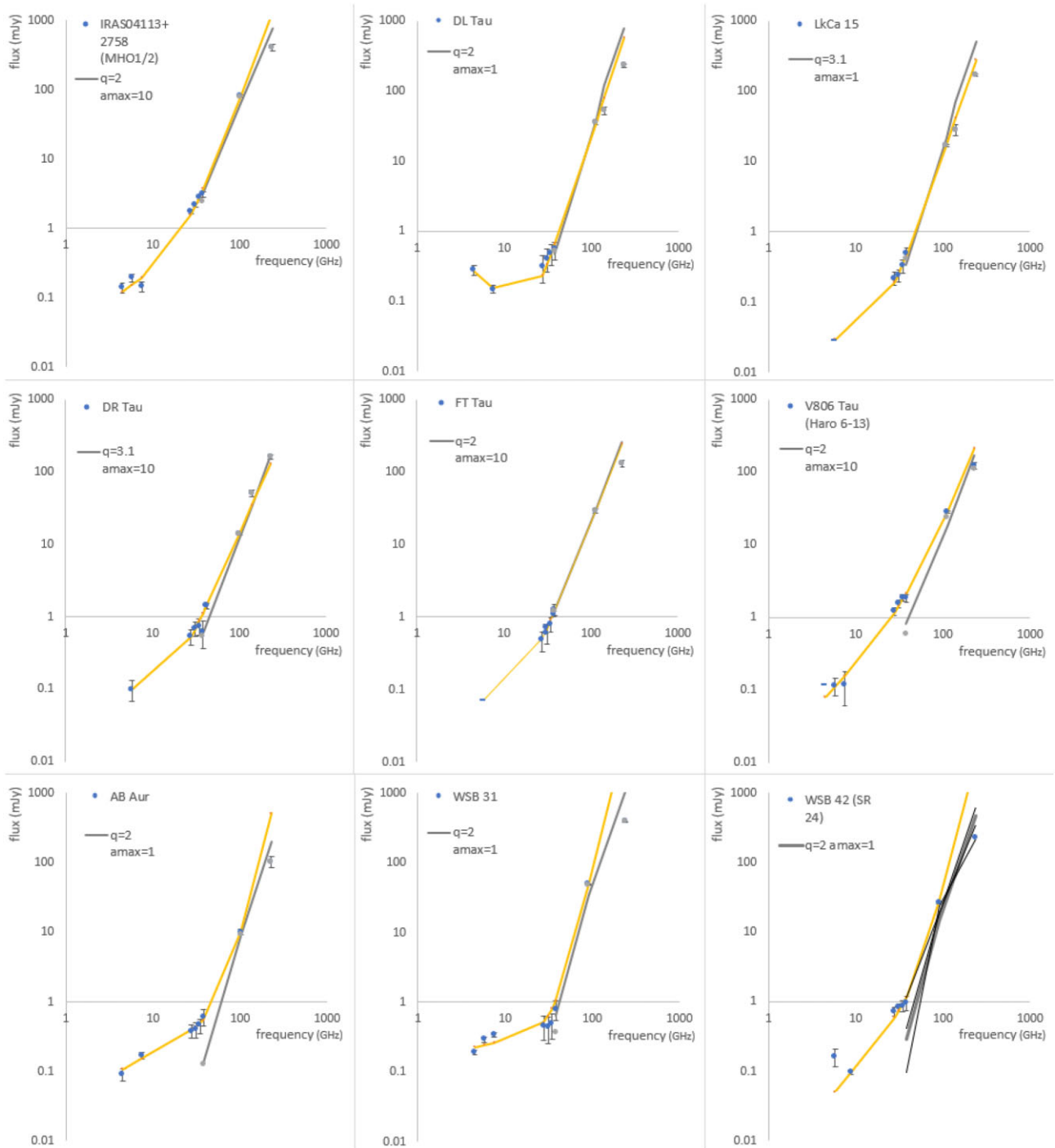


Figure 3. Spectral energy distributions of the nine systems in group (E), with sufficient good-quality flux measurement to fit spectral indices for dust and free–free emission. Yellow lines correspond to the empirical best fits listed in Table 4. The data compilation used is listed in Table A1; data points are shown here as blue circles with 1σ error bars. The grey lines are estimates for best fits using specified mass–opacity relations at wavelengths of 7.8 mm and ≈ 3 mm (frequencies of 38.25 and ≈ 100 GHz), with higher frequency fluxes used as secondary diagnostics (see text). These lines fit the data points in grey, where free–free emission (Table 4) has been subtracted. Grey points overlay blue points where the free–free contributions are small. In the legends, ‘amax’ refers to the largest grain radius (in mm) present in a population with a size index q (see text). In the lower-right plot, the fits with the three alternate q and amax combinations are also shown (thin black lines).

here (Table 5), the shift in inferred mass should be small. Ricci et al. derived $M(\text{dust})$ only, so we have applied the gas-to-dust mass ratio of Cuzzi et al. (2014), again for consistency with our work. Andrews & Williams (2005, 2007) fitted SEDs but finally used a generic $\kappa(1.3 \text{ mm})$ of $0.023 \text{ cm}^2 \text{ g}^{-1}$, with an implicit gas-to-dust mass ratio

of 100, 40 per cent higher than that in Cuzzi et al. (2014). The Cuzzi et al. (2014) values of $\kappa(1.3 \text{ mm})$ are only 30–70 per cent of the value adopted by Andrews & Williams (2005, 2007). Hence, if the Cuzzi et al. $\kappa(1.3 \text{ mm})$ were applied to observed fluxes, the $M(\text{disc}, 1.3 \text{ mm})$ would be inferred as ~ 1.5 –3 times higher.

Other factors in equation (1) are the dust temperature and source distance. The Planck function $B_\nu(T)$ is here for characteristic dust temperatures of 20 K (Andrews & Williams 2005, 2007), agreeing with predictions for the mid-plane at tens of au from the star (e.g. Chambers 2019). However, Ricci et al. (2010a,b) used system-specific models of mid-plane temperatures (not tabulated), so this could increase the scatter in the masses derived, over a fixed value.⁵ For uniformity with previous work, we adopted d of 140 pc to make our mass estimates, but checked parallaxes in *Gaia* Data Release 3 (early release) for any major discrepancies. There are three systems in our survey where accurate distances change the disc mass by ≥ 40 per cent: WSB 42 and GSS 39 in Ophiuchus are, respectively, only 100 and 110 pc distant, while DR Tau at 193 pc is at the far extent of the Taurus clouds. Effects on masses are noted in Table 5.

4 DISCUSSION

Our observations are ≥ 80 per cent complete⁶ for class II objects in Taurus and Ophiuchus, above fixed 1.3 mm flux thresholds. Owing to suspected contamination by anomalous microwave emission, and the difficulty of detecting weak dust signals at long wavelengths, we are only able to fit dust SEDs to ~ 30 per cent of our original sample of targets. Multiple frequency bands are clearly necessary to correctly identify and characterize dust in discs at radio wavelengths, as was also found to be the case for cloud cores (Mason et al. 2020).

For our best-fitting cases (black bars in Fig. 4), the disc masses using radio-regime data form a flatter distribution than earlier mass estimates based on shorter-wavelength data. (Our upper limits are less constraining, but show no cases where the disc mass is now thought to be reduced: white and shaded bars in Fig. 4.) Therefore, mass budgets available to form planets are inferred to be higher than previously thought, among our discs selected as millimetre bright. The median increase of $M(\text{disc}, 7.8 \text{ mm})$ over $M(\text{disc}, 1.3 \text{ mm})$ is a factor of ≈ 2.5 – however, this could be largely attributed to the use by Andrews & Williams (2005) of a higher κ -value than in more recent grain models. The 3 mm studies of Ricci et al. (2010a,b) are more self-consistent with our approach to dust properties, but have less sample overlap with our survey. For the three dust discs we also detect here, the increase in mass we find via K_a -band data is ~ 0.5 –1 dex.

At the left end of Fig. 4, around the disc mass ceiling of ~ 0.1 – 0.2 solar masses, different studies tend to converge in inferred disc mass, while at the faint end of the survey, AB Aur’s disc is now estimated at around 10 times more massive than before. This trend could support the finding of Ribas et al. (2020), from detailed disc modelling, that the optically thin assumption may not hold for observing wavelengths that are $\lesssim 1$ mm. Further modelling could test whether the convergence of mass estimates for the very brightest discs is still an artefact from high optical depth, even into the long-millimetre regime.

Whereas some of the discs we have characterized previously fell below a minimum-mass solar nebula of gas and dust (≈ 0.02 solar masses; Davis 2005), now they are all above twice this mass (Table 5).

⁵The parameters of their individual source models included stellar luminosity, effective temperature, and mass, plus disc surface density, surface density index, outer radius, grain size population index, and maximum grain size.

⁶Objects in the remaining 20 per cent include five targets we observed in unstable conditions (Table 2) and one lost from the source list (UZ Tau). Completeness refers to a base sample surveyed with millimetre/submillimetre photometry up to 2007. None of our target fields overlapped at GBT/ K_a -band resolution.

Table 5. Disc mass estimates (gas plus dust) for the 23 best-fitting disc systems, using wavelengths λ up to the limits in the three central columns. Systems are ordered by decreasing mass from the analyses (Andrews & Williams 2005, 2007) used in our sample selection. The maximum grain radius a_{max} is from our analysis (see text). System distances were set to 140 pc to match previous work (Ricci et al. 2010a,b). References for the stellar luminosities L_* (in a few cases, L_{bol}) include Bergner et al. (2020), Ribas et al. (2017), van der Marel et al. (2016), Salyk et al. (2013), Baldovin-Saavedra et al. (2011), McClure et al. (2010), and Enoch et al. (2009).

System	$M(\text{disc})$ (solar masses) for λ			a_{max} (mm)	L_* (L_\odot)
	$\leq 1.3 \text{ mm}$	$\leq 3 \text{ mm}$	$\leq 7.8 \text{ mm}$		
GG Tau	0.23		≤ 0.30	1	1.5
WSB 31	0.16	0.033	0.10	1	1.9
MHO 1/2	0.09		0.29	10	0.4
DL Tau	0.09	0.010	0.13	1	0.8
AS 209	0.052	0.009	≤ 0.26	1	1.4
LkCa 15	0.048		0.12	1 ^b	0.9
GSS 39 ^a	0.040	0.033	≤ 0.19	1	1.6
AS 205	0.033		≤ 0.44	1	2.5
WSB 60	0.032	0.11	≤ 0.04	10	0.3
DoAr 25	0.030	0.016	≤ 0.21	1	1.9
WSB 42 ^a	0.030		0.08	1	2.1
VSSG 23	0.030	0.0034	≤ 0.11	1	19
CI Tau	0.028	0.0086	≤ 0.04	1	1.0
GM Aur	0.025	0.011	≤ 0.12	1	0.8
DM Tau	0.024	0.0071	≤ 0.18	1	0.2
DR Tau ^a	0.019	0.0052	0.05	10 ^b	1.6
FT Tau	0.014		0.11	10	0.6
Haro 6-13	0.010		0.07	10	2.0
V892 Tau	0.009		≤ 0.36	1	88
DO Tau	0.007	0.016	≤ 0.08	10	1.2
CY Tau	0.006	0.012	≤ 0.25	1	0.5
AB Aur	0.0044		0.04	1	83
CW Tau	0.0024	0.0031	≤ 0.13	1	1.4

^aFor these systems, *Gaia* parallax indicates a distance significantly different to the adopted 140 pc; distance-corrected masses should be reduced by 40 per cent for WSB 42 and 50 per cent for GSS 39, and increased by 90 per cent for DR Tau.

^bThese systems were better fitted with size index $q = 3.1$; other fits use mass-opacity for $q = 2$.

The prior sub-MMSN examples are FT Tau, Haro 6-13, and AB Aur, in the first two of which there is now evidence for 1-cm-radius grains. Thus, the mass budget may be increased by accounting for larger particles. Compared with the Taurus discs modelled by Ribas et al. (2020), our long-wavelength data appear more successful in discovering large grains. After fitting SEDs out to 3 mm wavelengths, they find only 1 out of 23 systems to be consistent with the presence of 1-cm-radius grains, whereas our study finds 4 out of 23 cases. As only about a third of our systems are in Ophiuchus, our proportion of large-grain cases in the Taurus environment is higher again, at 4 out of 15.

These revised mass budgets still do not account for any ‘boulder’-sized, or larger, objects – such bodies are expected to contribute weak emission due to low surface areas relative to their mass, but can contribute significantly to the planet-forming potential. If grain growth through the centimetre-sized stages is fast, then this could potentially explain why we find rather few systems with ‘pebbles’.

The unbiased view from our flux-thresholded survey provides a useful comparison to radio-imaging studies, which necessarily focus on centimetre-bright discs. An unexpected result was that only a few discs in our millimetre-bright sample have yielded evidence of pebbles – in particular, only four systems have $\alpha(\text{dust}) \approx 3$ (within

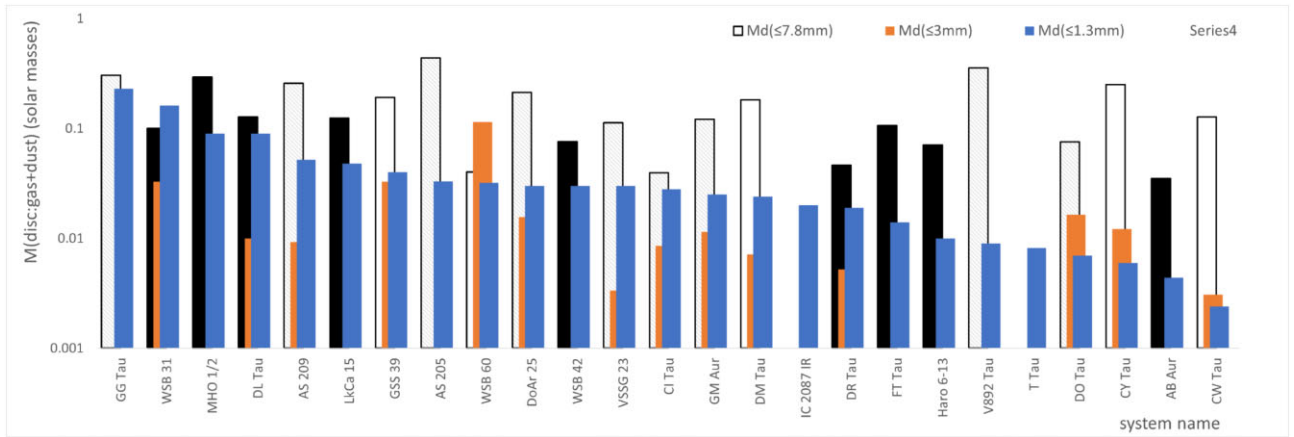


Figure 4. Distribution of disc masses, from the values listed in Table 5. Systems are ordered by decreasing mass from the surveys using data at up to 1.3 mm wavelength. The surveys up to 3 mm wavelength only covered part of this sample. Our results using wavelengths up to 7.8 mm are shown by the black-outlined bars: the solid black filled bars indicate good dust spectrum fits; the solid white filled bars are for upper limits on dust emission at 7.8 mm; and the bars with diagonal grey shading are also upper limits, for systems with suspected AME contamination.

10 per cent) and SEDs fitted with grains as large as 1 cm in radius. We find $\alpha(\text{dust}) \leq 3.3$ in at most one-quarter of the systems (6/23), even if we include limits just compatible with this value. There are no strong trends among the systems that do exhibit 1-cm-radius grains, but this is difficult to assess from such small numbers (e.g. a trend could easily be invalidated if one more system could be fitted). At modest significance, we note that none of the six large-grain candidates have host stars exceeding $2L_{\odot}$ (Table 5), and they also tend to be unusually single – only MHO 1/2 (where we treated the two discs as having identical dust properties) is a multiple, while e.g. Taurus’s multiplicity is ~ 62 per cent (Daemgen et al. 2015).

These results could indicate that centimetre-sized grains exist for only a small fraction of disc lifetimes, or that large grains form only in confined regions of the disc (limiting their contribution to photometric measurements). Disks@EVLA images of a few discs (e.g. Tazzari et al. 2016) indicate that the latter solution is plausible, but imaging of faint pebble emission far from the star is difficult. Disc theory (e.g. Birnstiel et al. 2016) indicates that centimetre-sized grains rapidly both drift inwards and fragment, so both solutions may coexist.

One surprising outcome is the apparent prevalence of anomalous microwave emission, with candidates comprising 40 per cent (10/25) of our targets. Greaves et al. (2018) discovered an association of AME with rare infrared spectral signatures of nanodiamonds, including in our GBT target V892 Tau. While slightly deeper radio data could confirm our candidate AME systems, detecting IR nanodiamond features in T-Tauri systems is likely to be very challenging (Acke & van den Ancker 2006). Greaves et al. (2018) suggested that AME correlates with stellar luminosity, but noted that this is not a sufficient condition for detection. For example, V892 Tau and AB Aur are similarly luminous (Table 5), but we cannot confirm AME around AB Aur (an upturn in flux is possible, but would be longwards of the K_a band; Table A1). Radio imaging is probably the most promising method to determine whether peaked radio spectra occur at particular locations in discs, giving clues to particles or mechanisms responsible.

Further radio photometry will help to determine when pebbles form. There has been long-standing interest in whether large grains could form at the cloud core stage, and most recently Mason et al.

(2020) have characterized SEDs using many spectral bands for the Orion Molecular Cloud (OMC2/3) regions. This study found *flatter* than expected dust spectra at 3 mm–1 cm wavelengths, suggesting a change in material state and thus in emissivity (e.g. Paradis et al. 2011). In contrast, we have found *steeper* spectra, with $\alpha(\text{dust}) \geq 2.7$, in our survey of Taurus and Ophiuchus. Photometric studies of further regions could help tie these findings together.

At least one disc system does exhibit a blackbody spectrum that extends out to very long wavelength: DG Tau A has $\alpha(\text{dust}) \approx 2.1$ out to 4.5 cm (Hesterly et al. in preparation). This star is very young (around 0.6 Myr), and so may be a linking case to the protostellar disc systems that are known to have higher dust masses. Tychoniec et al. (2020) inferred 10 times more dust mass in class 0 versus class II objects, in various regions, using data up to 9 mm. They inferred that the solid content of giant exoplanets could then be provided if it is gathered with ~ 15 per cent efficiency, similar to the earlier estimate of ~ 10 per cent from Greaves & Rice (2011). The VANDAM project is surveying protostellar discs in Orion out to 9 mm wavelength, reaching similar conclusions about high dust masses (Tobin et al. 2020, and references therein).

The recent finding (Galametz et al. 2019) of low $\beta_{1-3\text{mm}}$ values in protostellar envelopes suggests that grains can start to grow surprisingly early, before reaching the denser disc environment, perhaps connecting to altered properties even at the pre-stellar core stage (Mason et al. 2020). In the future, following the balances of dust sizes from pre-stellar cores to class II/HAe discs can shed more light on how large quantities of solids are fed to growing planets. In this context, we note that further GBT- K_a photometry is in hand, for a sample of class I systems in Taurus and Ophiuchus.

On the theoretical side, Drażkowska, Stammer & Birnstiel (2021) find that fragmentation may actually be beneficial to planetary growth, as it could maintain a longer-lasting flow of small pebbles. Where the fragmentation threshold velocity is higher, dust grains tend to grow larger, reaching above centimetre sizes at tens of au in only 2×10^5 yr. Hence, we postulate that if grains always tend to fragment at similar speeds, pebble growth might be hampered around more massive stars where grains are orbiting faster (for the same radius). This could match with our finding that the six large-grain systems (Table 5) have low-luminosity host stars.

5 CONCLUSIONS

A systematic 1-cm-band photometric survey is analysed to search for evidence of large dust grains in millimetre-bright protoplanetary discs. At most, a quarter of the discs have any evidence of having formed ‘pebbles’. This suggests that drift/fragmentation barriers to pebble formation found in disc theory do in fact occur in real discs. A higher proportion of the systems (up to 40 per cent) have indications of anomalous microwave emission, likely from spinning nanoparticles, including the first such candidates with low-luminosity host stars. This result was unexpected, and so it is desirable to further examine populations of both nano- and centimetre-scale particles, over the evolution from cloud cores to young stars.

ACKNOWLEDGEMENTS

We thank co-observer Alexis Smith. Regression analysis was performed with the REAL STATISTICS PACKAGE, author Charles Zaiontz. The Green Bank Observatory is a facility of the National Science Foundation operated under cooperative agreement by Associated Universities, Inc.

DATA AVAILABILITY

The GBT project ID was AGBT07A-038 and the raw data can be obtained through the NRAO public archive. The processed photometric results are fully tabulated in Appendix A.

REFERENCES

- Acke B., van den Ancker M. E., 2006, *A&A*, 457, 171
 André P., Montmerle T., 1994, *ApJ*, 420, 837(A94)
 Andrews S. M., Williams J. P., 2005, *ApJ*, 631, 1134(A05)
 Andrews S. M., Williams J. P., 2007, *ApJ*, 671, 1800(A07)
 Baldovin-Saavedra C. et al., 2011, *A&A*, 528, 22
 Balser D. S., Nikolic B., Prestage R. M., 2006, PTCS Project Note 49.1. Available at: <https://safe.nrao.edu/wiki/bin/view/GB/PTCS/ProjectNotes>
 Beckwith S. V. W., Sargent A. I., Chini R. S., Guesten R., 1990, *AJ*, 99, 924(B90)
 Bergner J. B. et al., 2020, *ApJ*, 898, 97
 Birnstiel T., Fang M., Johansen A., 2016, *Space Sci. Rev.*, 205, 41
 Chambers J., 2019, *ApJ*, 879, 98
 Chandler C., 2007, *Transnational Science with ALMA: Through Disks to Stars and Planets*. National Radio Astronomy Observatory, p. 34 Available at: www.cv.nrao.edu/naasc/disk07
 Cuzzi J. N., Estrada P. R., Davis S. S., 2014, *ApJS*, 210, 21
 d’Alessio P., Calvet N., Hartmann L., 2001, *ApJ*, 553, 321
 Daemgen S., Bonavita M., Jayawardhana R., Lafrenière D., Jansun M., 2015, *ApJ*, 799, 155
 Davis S. S., 2005, *ApJ*, 627, L153
 Draine B., 2006, *ApJ*, 636, 1114
 Drażkowska J., Stammer S. M., Birnstiel T., 2021, *A&A*, 647, A15
 Dzib S. et al., 2013, *ApJ*, 775, 63(D13)
 Dzib S. et al., 2015, *ApJ*, 801, 91(D15)
 Enoch M., J. Evans N., II, Sargent, A. I., Glenn J., 2009, *ApJ*, 692, 973
 Furlan E., 2011, *ApJS*, 195, 3
 Galametz M., Maury A. J., Valdivia V., Testi L., Belloche A., André Ph., 2019, *A&A*, 632, 5
 Greaves J. S. et al., 2018, *Nat. Astron.*, 2, 662
 Greaves J. S., 2007, *SISSA Proc. Sci.*, id61
 Greaves J. S., Rice W. K. M., 2010, *MNRAS*, 407, 1981
 Greaves J. S., Rice W. K. M., 2011, *MNRAS*, 412, L88
 Guilloteau S. et al., 2011, *A&A*, 529, 105
 Harris R. J., 2013, PhD thesis, Harvard Univ.

- Kitamura Y. et al., 2002, *ApJ*, 581, 357(K02)
 Kwon W., Looney L. W., Mundy L. G., J. Welch W., 2015, *ApJ*, 808, 102(K15)
 Lommen D. et al., 2009, *A&A*, 495, 869
 Majid W., Bagri D., 2006, *Interplanetary Network Progress Report* 42-165. p. 1
 Manara C. F., Morbidelli A., Guillot T., 2018, *A&A*, 618, L3
 Mannings V., 1994, *MNRAS*, 271, 587(M94)
 Mason B. et al., 2020, *ApJ*, 893, 13
 McClure M. K. et al., 2010, *ApJS*, 188, 75
 Motte F., André P., 2001, *A&A*, 365, 440(M01)
 Motte F., André P., Neri R., 1998, *A&A*, 336, 150 (M98)
 Najita J. R., Kenyon S. J., 2014, *MNRAS*, 445, 3315
 Nuernberger D., Brandner W., Yorke H. W., Zinnecker H., 1998, *A&A*, 330, 549(N98)
 Osterloh M., Beckwith S. V. W., 1995, *ApJ*, 439, 288
 Paradis D., Bernard J.-P., Mény C., Gromov V. 2011, *A&A*, 534, 118
 Pérez L. M., et al., 2015, *ApJ*, 813, 41
 Perley R. A., Butler B. J., 2013, *ApJS*, 204, 19
 Piétu V. et al., 2006, *A&A*, 460, L43(P06)
 Pollack J. B. et al., 1994, *ApJ*, 421, 615
 Ribas A. et al., 2017, *ApJ*, 849, 63
 Ribas A. et al., 2020, *A&A*, 642, 171
 Ricci L., Testi L., Natta A., Brooks K. J., 2010b, *A&A*, 521, 66(R10b)
 Ricci L., Trotta F., Testi L., Natta L., Isella A., Wilner D. J., 2012, *A&A*, 540, 6(R12)
 Ricci L., Testi L., Natta A., Neri R., Cabrit S., Herczeg G. J., 2010a, *A&A*, 512, 15(R10a)
 Salyk C., Herczeg G. J., Brown J. M., Blake G. A., Pontoppidan K. M., van Dishoeck E. F., 2013, *ApJ*, 769, 21
 Simon M., Guilloteau S., 1992, *ApJ*, 397, L47(S92)
 Tazzari M. et al., 2016, *A&A*, 588, 53(T16)
 Tobin J. J., et al., 2020, *ApJ*, 890, id130
 Tokuda K. et al., 2020, *ApJ*, 899, 10(T20)
 Tychoniec L. et al., 2020, *A&A*, 640, 19
 Ubach C., Maddison S. T., Wright C. M., Wilner D. J., Lommen D. J. P., Koribalski B., 2017, *MNRAS*, 466, 4083
 van der Marel N., Verhaar B. W., van Terwisga S., Merín B., Herczeg G., Ligterink N. F. W., van Dishoeck E. F. 2016, *A&A*, 592, 126
 Zapata L., Rodríguez L. F., Palau A., 2017, *ApJ*, 834, 138

APPENDIX A: GBT DATA DETAILS

A1 Compilation of fluxes

Table A1 lists the flux data used in fitting spectral energy distributions, from our GBT observations and from the literature. The sources are listed by order of observation, which was with Tau preceding Oph, and then in order of decreasing 1.3 mm flux. (IC 2087 IR is listed in observing-sequence order, but our flux estimate of the time has been replaced by a subsequent measurement).

The facilities used include single dishes, GBT 100 m (this work), IRAM (Institut de RadioAstronomie Millimétrique) 30 m, and JCMT (James Clerk Maxwell Telescope) 15 m, and interferometers, ALMA-ACA (Atacama Large Millimeter/submillimeter Array – ALMA Compact Array), ATCA (Australia Telescope Compact Array), CARMA (Combined Array for Research in Millimeter-wave Astronomy), NMA (Nobeyama Millimeter Array), PdBI (Plateau de Bure Interferometer), and VLA (Very Large Array).

References for the literature data are as follows: André & Montmerle (1994; hereafter A94); Andrews and Williams (2005, 20A07; hereafter A05, A07); Beckwith et al. (1990; hereafter B90); Dzib et al. (2013, 2015; hereafter D13 and D15); Guilloteau et al. (2011; hereafter G11); Kitamura et al. (2002; hereafter K02); Kwon et al. (2015; hereafter K15); Mannings (1994; hereafter M94); Motte,

Table A1. Flux data compilation; references and facilities are listed in Appendix A, Section A1.

object	flux (mJy)	error (mJy)	freq. (GHz)	reference	facility
GG Tau	1.04	0.06	27.75		
	1.06	0.08	31.25		
	1.09	0.12	34.75		
	1.00	0.18	38.25		
	90	9	116 S92	PdBI	DM Tau
	593	53	230 B90/A05	IRAM-30m	
IRAS 04113+2758 (MHO 1/2)	0.141	0.022	4.5 D15	VLA	
	0.146	0.025	7.5 D15	VLA	
	1.75	0.13	27.75		
	2.22	0.16	31.25		
	2.83	0.21	34.75		
	3.14	0.29	38.25		
	81	2	102.5 R12	CARMA	AB Aur
	410	40	240 M01/A05	IRAM-30m	
T Tau	16.50	1.70	4.5 D15	VLA	
	5.31	1.72	7.5 D15	VLA	
	13.21	0.11	27.75		
	13.26	0.11	31.25		
	12.99	0.12	34.75		
	11.95	0.21	38.25		
	48.8	10	110 G11	PdBI	CW Tau
	280	9	230 B90/A05	IRAM-30m	
GM Aur	0.27	0.08	27.75		
	0.34	0.06	31.25		
	0.41	0.10	34.75		
	0.17	0.23	38.25		
	23.7	0.8	110 G11	PdBI	AS 205
	37	4	141 K02	NMA	
	253	12	230 B90/A05	IRAM-30m	
V892 Tau	0.375	0.034	4.5 D15	VLA	
	0.421	0.051	7.5 D15	VLA	
	1.61	0.15	27.75		
	1.82	0.17	31.25		
	1.85	0.17	34.75		
	1.17	0.15	38.25		
	54.9	1.0	102.5 R12	CARMA	WSB (EI 24) 31
	234	19	230 M94/A05	JCMT-15m	
DL Tau	0.278	0.045	4.5 D15	VLA	
	0.147	0.018	7.5 D15	VLA	
	0.31	0.14	27.75		
	0.40	0.15	31.25		
	0.48	0.16	34.75		
	0.54	0.15	38.25		
	35.0	2.4	113 K15	CARMA	GSS (EI 27) 39
	52	6	141 K02		
	230	14	240 M01/A05	IRAM-30m	
CI Tau	0.16	0.08	27.75		
	0.22	0.06	31.25		
	0.18	0.09	34.75		
	0.01	0.12	38.25		
	28.3	1.5	113 K15	CARMA	AS 209
	190	17	230 B90/A05	IRAM-30m	
					DoAr 25
LkCa 15	0.22	0.04	27.75		
	0.24	0.05	31.25		
	0.33	0.07	34.75		
	0.50	0.09	38.25		
	17.0	0.8	110 P06	PdBI	WSB (SR 24 A/S) 42
	28	5	141 K02	NMA	
	167	6	240 O95/A05	IRAM-30m	
DR Tau	0.53	0.13	27.75		
	0.68	0.15	31.25		
	0.73	0.19	34.75		
	0.62	0.26	38.25		
	13.9	0.5	101 R10a	PdBI	VSSG (SR 21 A) 23
	51	6	141 K02	NMA	
	159	11	230 B90/A05	IRAM-30m	
IC 2087 IR (IRAS 04369+2539)	0.220	0.016	4.5 D15	VLA	
	0.356	0.014	7.5 D15	VLA	
	2.08	0.17	27.75		
	2.42	0.19	31.25		
	2.70	0.20	34.75		
	3.04	0.25	38.25		
		0.9	102.5 R12	CARMA	WSB 60
			225 T20	ALMA-ACA	
DO Tau	201	1	225 T20	ALMA-ACA	
	0.52	0.11	27.75		
	0.82	0.12	31.25		
	1.05	0.11	34.75		
	0.88	0.18	38.25		
	30.8	1.3	113 K15	CARMA	
	37	5	141 K02	NMA	
	138	11	230 B90/A05	IRAM-30m	
CY Tau	-0.05	0.11	27.75		
	0.17	0.12	31.25		
	0.45	0.12	34.75		
	0.83	0.18	38.25		
	0.27	0.29	33		
	26.1	3.9	110 R10a	PdBI	
	32	4	141 K02	NMA	
	133	11	230 B90/A05	IRAM-30m	
FT Tau	u.l.	0.024	6 T15	VLA	
	0.48	0.15	27.75		
	0.59	0.17	31.25		
	0.80	0.18	34.75		
	1.27	0.23	38.25		
	28.8	2.0	113 K15	CARMA	
	130	14	230 B90/A05	IRAM-30m	
Haro 6-13 (V806 Tau)	0.070	0.120	4.5 D15	VLA	
	0.121	0.060	7.5 D15	VLA	
	1.21	0.16	27.75		
	1.56	0.19	31.25		
	1.85	0.20	34.75		
	1.84	0.24	38.25		
	28.7	1.0	113 K15	CARMA	
	124	13	230 B90/A05	IRAM-30m	

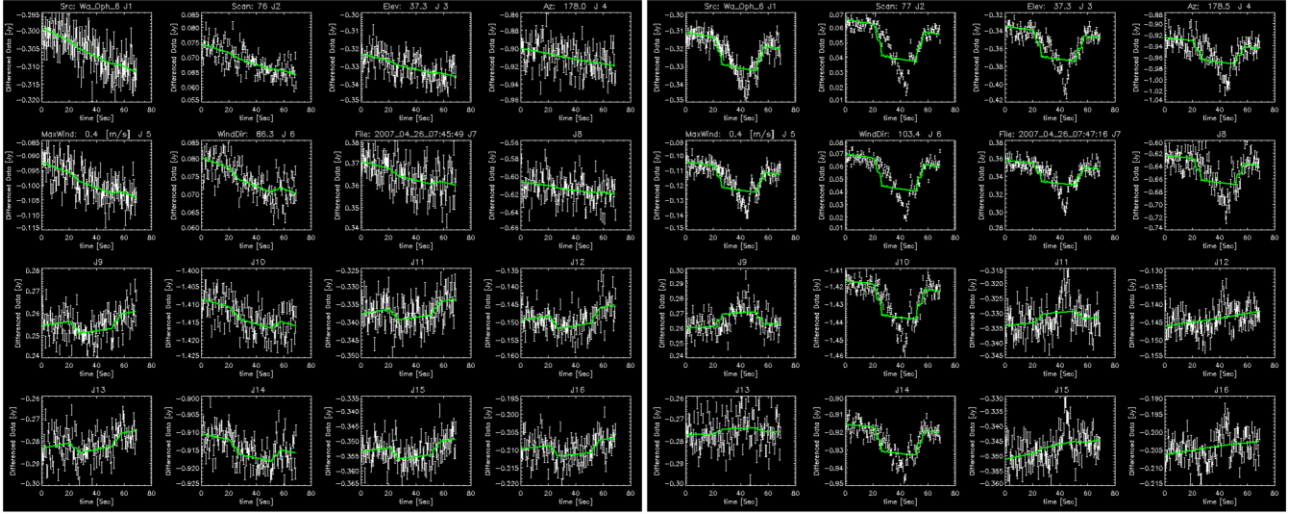


Figure A1. Examples of calibrated observations in different conditions. The first two observations of WaOph 6 are shown; the second (right-hand panel) was rejected.

André & Neri (1998; hereafter M98) and Motte & André (2001; hereafter M01); Nuernberger et al. (1998; hereafter N98); Osterloh & Beckwith (1995; hereafter O95); Piétu et al. (2006; hereafter P06); Ricci et al. (2010a, 2010b, 2012; hereafter R10a, R10b, R12); Simon & Guilloteau (1992; hereafter S92); Tazzari et al. (2016; hereafter T16); Tokuda et al. (2020; hereafter T20).

A2 Rejected data

Differenced data were visually examined for each observation. Five Ophiuchus sources, the last observed, were rejected for scientific analysis as some of the signals were seen to vary erratically over time. Fig. A1 shows an example of the first two observations made of WaOph 6. The differenced data can be fitted in the first observation (left-hand panel, green curves) but there are sharp signal changes in the second observation (right-hand panel) that cannot be fitted.

Table A2 lists the mean fluxes by subband after removal of the rejected observations (as listed in Table 3). We note that LFAM 30 was observed in error, instead of the intended target LFAM 3. This does not affect survey completeness, as both objects are now classified as outside our class II criterion; they are respectively class I and FS (flat-spectrum) objects.

Table A2. Subband data for the five rejected sources, after removal of the bad observations (noted in Table 3).

object	flux (mJy)	error (mJy)	freq. (GHz)
WaOph 6	1.31	0.37	27.75
	1.49	0.60	31.25
	2.58	2.63	34.75
	1.54	0.88	38.25
GSS 26	-0.16	1.26	27.75
	0.87	2.69	31.25
	2.55	4.96	34.75
DoAr 44	-0.82	2.96	38.25
	1.40	5.73	27.75
	3.48	15.57	31.25
	8.07	31.87	34.75
LFAM 30	-1.47	7.79	38.25
	1.28	0.93	27.75
	1.47	2.23	31.25
	0.66	3.38	34.75
RNO 91	2.65	1.20	38.25
	1.63	1.23	27.75
	2.94	2.85	31.25
	5.00	5.30	34.75
	0.67	1.31	38.25

This paper has been typeset from a $\text{\TeX}/\text{\LaTeX}$ file prepared by the author.